Constructing three-dimensional porous Ni/Ni$_3$S$_2$ nano-interfaces for highly active hydrogen evolution catalysis in neutral and alkaline media

Yiming An,[a] Bolong Huang,*[b] Zilong Wang,[a] Xia Long, [a] Yongcai Qiu,[a,c] Jue Hu,[a] Shihe Yang*[a]

[a] Department of Chemistry, The Hong Kong University of Science and Technology, Clear Water Bay, Kowloon, Hong Kong, China.
E-mail: chsyang@ust.hk

[b] Department of Applied Biology and Chemical Technology, The Hong Kong Polytechnic University, Hong Hum, Kowloon, Hong Kong, China
E-mail: bhuang@polyu.edu.hk

[c] Department of Electronic Engineering, The Chinese University of Hong Kong, Shatin, New Territories, Hong Kong, China.

Abstract

It is still a challenging issue to design earth-abundant catalysts with high activity, stability and low cost for hydrogen evolution reaction from water splitting in alkaline and neutral solutions. Here, we report a facile synthesis route of three-dimensional porous Ni/Ni$_3$S$_2$ nano-network on carbon cloth for efficient hydrogen evolution. This unique structure exposes a high proportion of Ni/Ni$_3$S$_2$ hetero-interface to electrolyte, creating a synergetic effect between Ni and Ni$_3$S$_2$ for enhancing HER as verified by DFT calculation. The resulting porous network shows a high HER activity in alkaline media, reaching 10 mA/cm^2 at 95 mV with a tafel slope of 67 mV/dec, which is much smaller than that of nickel material being used in industry.

Introduction

Electrocatalysis is a scalable and efficient way to realizing water to hydrogen conversion with inputs of only electricity and water.[1] The most efficient electrocatalysts for hydrogen evolution reaction (HER) nowadays remain platinum (Pt) group metals with negligible overpotential and very small tafel slope in acidic solutions.[2] However, the large scale applications of these catalysts are greatly limited by their high cost and scarcity, as well as the low performance of these catalysts in alkaline solutions.[3] Though many active, stable, and non-precious metal electrocatalysts such as MoS$_2$, WS$_2$, NiSe, CoP, etc.,[4-8] have been reported recently, they only showed ideal performance toward HER in acidic electrolytes. And their activity in neutral and alkaline medium, is usually two to three orders of magnitude lower.[9] Therefore, designing efficient but low-cost electrocatalysts for HER in neutral and alkaline electrolyte is still one of the most challenging issues in order to couple HER with OER to realize overall water splitting in the same pH range.

Nickel (Ni) shows relatively high catalytic activity in alkaline electrolyte, which is commonly used in industrial alkaline electrolyzers for catalyzing water reduction nowadays.[10, 11] But the catalytic properties are unsatisfactory because of its high overpotential and large Tafel slope.[12] Much research has focused on promoting the HER activities of Ni-based materials in alkaline
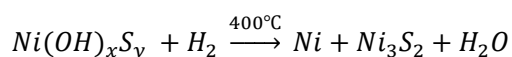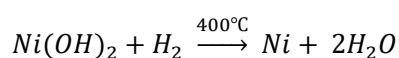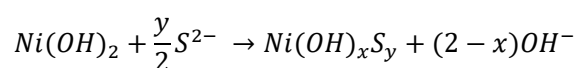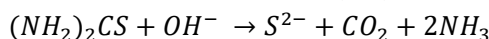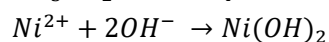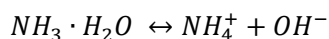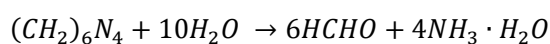
solution, including nanostructuring, forming alloys, and constructing heterostructures, etc..[13-15] Transition metal sulfides are another sort of HER active material which are widely studied as alternative noble metal free catalysts for water splitting,[16-19] however, the moderate HER catalytic activity, low electrical conductivity, and complex fabrication procedure greatly limit their application. Among transition metal sulfide species, Ni_3S_2 stands out for its intrinsic metallic property and thus its more fluent charge transfer than many other transition metal sulfides.[20, 21]

Currently, the studies of Ni sulfide (NiS) electrocatalysts have been mainly directed on variation of the sulfide species[17, 22] and the corresponding different morphologies grown on Ni substrates[20, 23, 24]. However, the catalytic activity is not satisfactory in alkaline/neutral environment due to the limitation of intrinsic catalytic activity and exposed active sites. We propose in the present work that the electrocatalytic activity of Ni/NiS can be effectively promoted by constructing a porous framework with large Ni/NiS interfaces through nanostructuring in three-dimensions (3D). Banking on advantages of both Ni metal and metallic Ni_3S_2, we have developed a facile two-step synthetic approach to producing a novel 3D porous Ni/Ni_3S_2 (P-Ni/Ni_3S_2) nanostructured catalyst, which could not only conquer the synthetic complexity but also expose sufficient Ni/Ni_3S_2 interface to electrolyte for synergetic catalytic effects. This unique design affords good flexibility, stability, binder-free property, and more importantly, remarkable electrocatalytic properties for HER in neutral and alkaline media with a very small overpotential of 95 mV and 196 mV, respectively, at current density of 10 mA/cm^2, as well as a low Tafel slope of 67 mV/dec and 170 mV/dec.

Results and discussion

Synthesis and characterizations of the catalyst.

The P-Ni/Ni_3S_2 based catalytic electrode was fabricated by reducing $Ni(OH)_xS_y$ nanosheets, which was hydrothermally grown on oxidized carbon cloth, at 400 ℃ for an hour in H_2 atmosphere (see SI for further details). In the reaction system, $Ni(OH)_2$ has priority of initial growth, followed by the formation of sulfide at the outer shell. Specifically, the sulfide ions gradually diffuse onto the $Ni(OH)_2$ surface, causing ion exchange due to the relatively low K_{sp} of nickel sulfide (3.0*10^{-21}) compared with that of $Ni(OH)_2$ (2.8*10^{-16}). The ion exchange process is further confirmed by two step hydrothermal sulfurization of $Ni(OH)_2$ (Figure S1).

$$(CH_2)_6N_4 + 10H_2O \rightarrow 6HCHO + 4NH_3 \cdot H_2O$$
$$NH_3 \cdot H_2O \leftrightarrow NH_4^+ + OH^-$$
$$Ni^{2+} + 2OH^- \rightarrow Ni(OH)_2$$
$$(NH_2)_2CS + OH^- \rightarrow S^{2-} + CO_2 + 2NH_3$$
$$Ni(OH)_2 + \frac{y}{2}S^{2-} \rightarrow Ni(OH)_xS_y + (2-x)OH^-$$

$$Ni(OH)_2 + H_2 \xrightarrow{400℃} Ni + 2H_2O$$
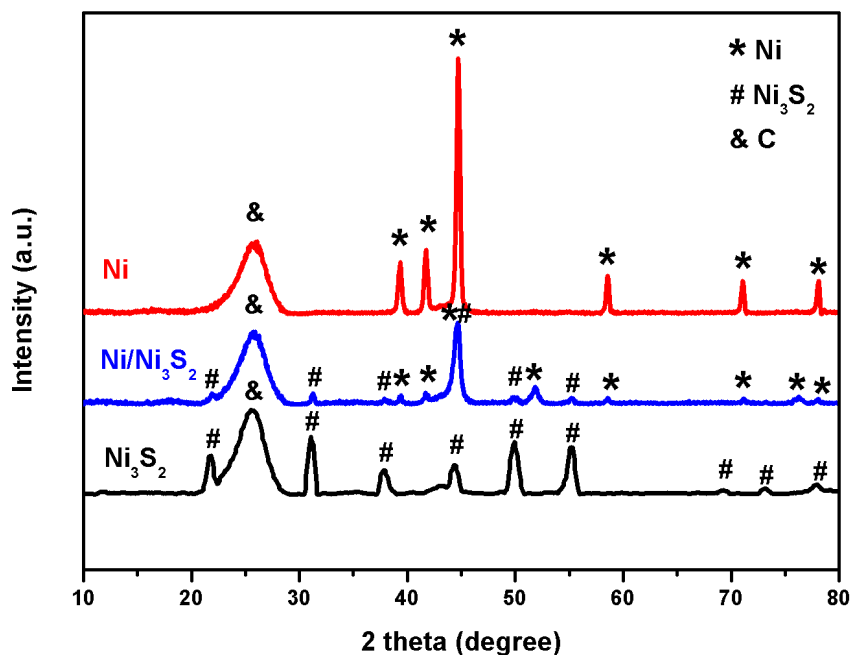
$$Ni(OH)_xS_y + H_2 \xrightarrow{400℃} Ni + Ni_3S_2 + H_2O$$

Figure 1. XRD patterns of pure Ni, pure Ni₃S₂, and P-Ni/Ni₃S₂ on carbon cloth. XRD peaks of P- P-Ni/Ni₃S₂ (blue curve) can be marked as hexagonal Ni, cubic Ni and hexagonal Ni₃S₂.

The X-ray diffraction (XRD) pattern of pure Ni, pure Ni_3S_2 and P-Ni/Ni_3S_2 grown on oxidized carbon cloth (OCC) is shown in Figure 1. It clearly reveals that P-Ni/Ni_3S_2 structure obtained by Ni(OH)$_x$S$_y$ nanosheets reduction contains Ni and metallic Ni_3S_2 without impure species. P-Ni/Ni_3S_2 (blue curve in Figure 1) shows XRD peaks consistent with peaks of hexagonal Ni_3S_2, and two phases of Ni---hexagonal and cubic phases. The diffraction peaks of 2θ = 39.1°, 41.5° and 44.5° correspond to (010), (002) and (011) crystal planes of hexagonal Ni. Pure Ni in Figure 1 (red curve) is hexagonal, while metal Ni in P-Ni/Ni_3S_2 (blue curve in Figure 1) contains not only hexagonal but also cubic phase, 2θ = 44.5°, 51.8°, 76.4° and 92.9° refer to cubic Ni planes of (111), (200), (220), (311). 2θ = 21.7, 31.1, 37.8, 38.3 and 44.3 are ascribed to (010), (110), (003), (021) and (202) planes of hexagonal Ni_3S_2, respectively. All the peaks shown in blue curve (P-Ni/Ni_3S_2) can be attributed to Ni and Ni_3S_2, indicating the successful conversion of Ni(OH)$_x$S$_y$ precursor to P-Ni/Ni_3S_2.
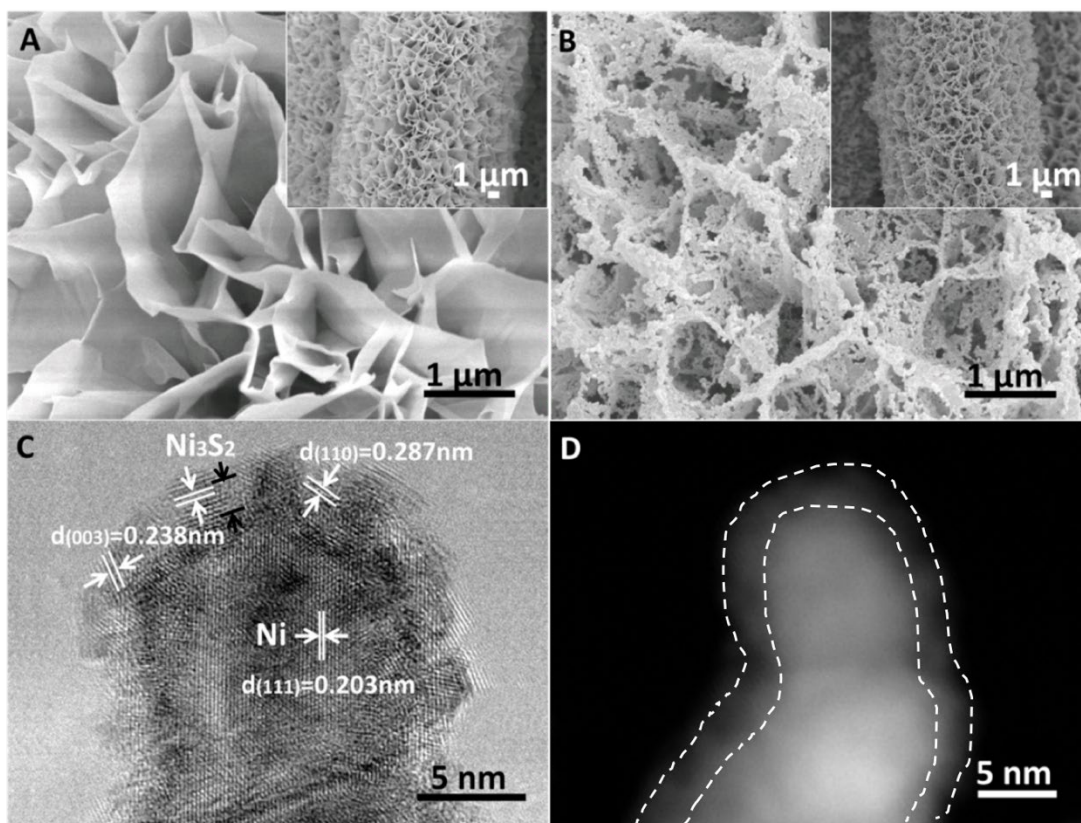
Figure 2. Morphology and structure characterizations. SEM images of A) Ni(OH)$_x$S$_y$ nanosheet precursor B) P-Ni/Ni$_3$S$_2$ obtained by reduction of Ni(OH)$_x$S$_y$ nanosheets C) HRTEM image showing the typical structure of P-Ni/Ni$_3$S$_2$ (small grains of Ni$_3$S$_2$ wrapping around Ni metal) D) STEM dark-field image of P-Ni/Ni$_3$S$_2$, showing the brightness of about 2 nm thick Ni$_3$S$_2$ containing outer shell differs from the inner Ni framework.

Scanning electron microscopy (SEM) and high resolution transmission electron microscopy (HRTEM) was used to investigate the structures of as synthesized materials. The morphology change of Figure 2A to figure 2B shows the conversion of Ni(OH)$_x$S$_y$ nanosheet precursor to porous Ni/Ni$_3$S$_2$ structure. The Ni(OH)$_x$S$_y$ nanosheets are several nanometers thick, and micro-scale in diameter. The nanosheets are standing perpendicularly on oxidized carbon cloth (OCC), forming a well-connected flower-like structure. The reduced product P-Ni/Ni$_3$S$_2$ maintains the structure of Ni(OH)$_x$S$_y$ in macroscopic scale, while forming little pores and branches in it. HRTEM shows that Ni branches are covered with both Ni and Ni$_3$S$_2$ containing outer shell, forming a capsule structure. Most of the Ni$_3$S$_2$ particles in outer shell exhibit lattice fringes of (003) planes with characteristic d value of 0.238 nm, some of (110) plane with d=0.287nm could also be found as it is demonstrated in Figure 2C. The inter core is dominated by Ni cubic (111) and hexagonal (011) plane, which refers to the same d value 0.203nm, in accordance with the strongest peak shown in XRD pattern. Ni framework is single crystal with consecutive crystal lattice according to the HRTEM image, while small grains of Ni$_3$S$_2$ is not uniformly wrapping around Ni framework, exposing Ni/Ni$_3$S$_2$ interface while catalyzing HER reaction. Dark field scanning transmission electron microscopy (STEM) is employed to confirm the structure of P-Ni/Ni$_3$S$_2$. The brightness of about 2 nm thick outer shell differs from the inner Ni framework (corresponds to black arrow pattern in figure 2C), forming an obvious boundary, which could also
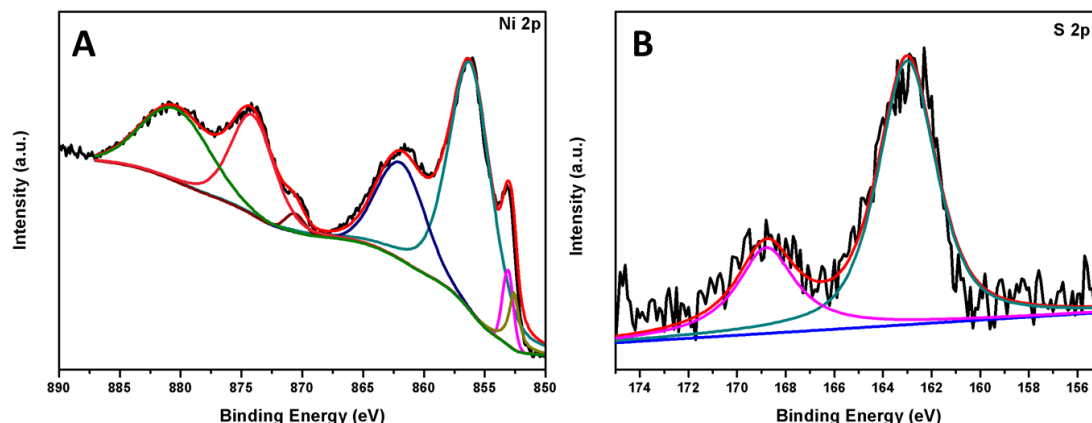
be discovered in HRTEM image.

Figure 3. XPS spectra of A) Ni 2p peaks and B) S 2p peaks for P-Ni/Ni$_3$S$_2$, revealing the existence of Ni^0(green curve in Figure 3A), Ni$^{\delta +}$(pink curve in Figure 3A), Ni^{2+} (cyan curve in Figure 3A) and S$^{\delta -}$ (Figure 3B) on P-Ni/Ni$_3$S$_2$ surface.

X-ray photoelectron spectroscopy (XPS) is employed to characterize the surface chemistry of P-Ni/Ni$_3$S$_2$, confirming the existence of Ni and S in the structure. The Ni 2p XPS spectrum shows characteristic peaks for metallic Ni^0, Ni$^{\delta +}$ and Ni^{2+}. The Ni 2p1/2 and Ni 2p3/2 show peaks at 874.1 eV and 856.2 eV, respectively. The peaks around 852.6 eV and 870.6 eV for Ni 2p3/2 and Ni 2p1/2 are attributed to metallic Ni on the surface. The characteristic peak of Ni$_3$S$_2$ lies at 853.1 eV, which is positively shifted by 0.5 eV compared with metallic nickel peak at 852.6 eV. In the XPS spectra of S (Figure 3B), two peaks located at 163.0 eV and 168.8 eV are observed, revealing the S$^{\delta -}$ in Ni$_3$S$_2$ and some oxidation states of Ni$_3$S$_2$ caused by exposing in the air.

Electrocatalytic performance.

High surface area is beneficial for robust electrocatalyst design because electrocatalytic activity trend matches the same trend with electrochemical surface area (ECSA) for a certain catalyst. To promote the electrocatalytic activity of Ni-based material toward HER, firstly, we consider construct 3D porous network by reducing Ni-based hydroxide nanosheets, which possesses larger ECSA compared with other Ni material such as Ni foil and Ni foam. For the electrochemical characterizations in 1 M KOH, reference and counter electrode are Ag/AgCl and platinum (Pt) wire, respectively. Electrocatalysts grown on OCC served as working electrode. Electrochemical double layer capacitances were measured to characterize the ECSA by cyclic voltammetry method, which could be related to catalytic activity. The double-layer capacitance (C$_{dl}$) is half the slope of charging current density difference against scan rate. From Figure 4D, 3D porous Ni shows the highest ECSA with C$_{dl}$ = 2.6 uF, nearly 7 times higher than electrodeposited Ni particle. Attributing to the high ECSA, 3D porous Ni outperforms Ni particle electrodeposited on OCC by 21 mV at current density of 10 mA/cm^2, while oxidized carbon cloth shows no HER activity with negligible current density in the test range (Figure 4A). The enlargement of ECSA leads to more catalytic active sites exposed in the reaction per unit area, confirming the effectiveness of 3D structure construction and nanostructuring.
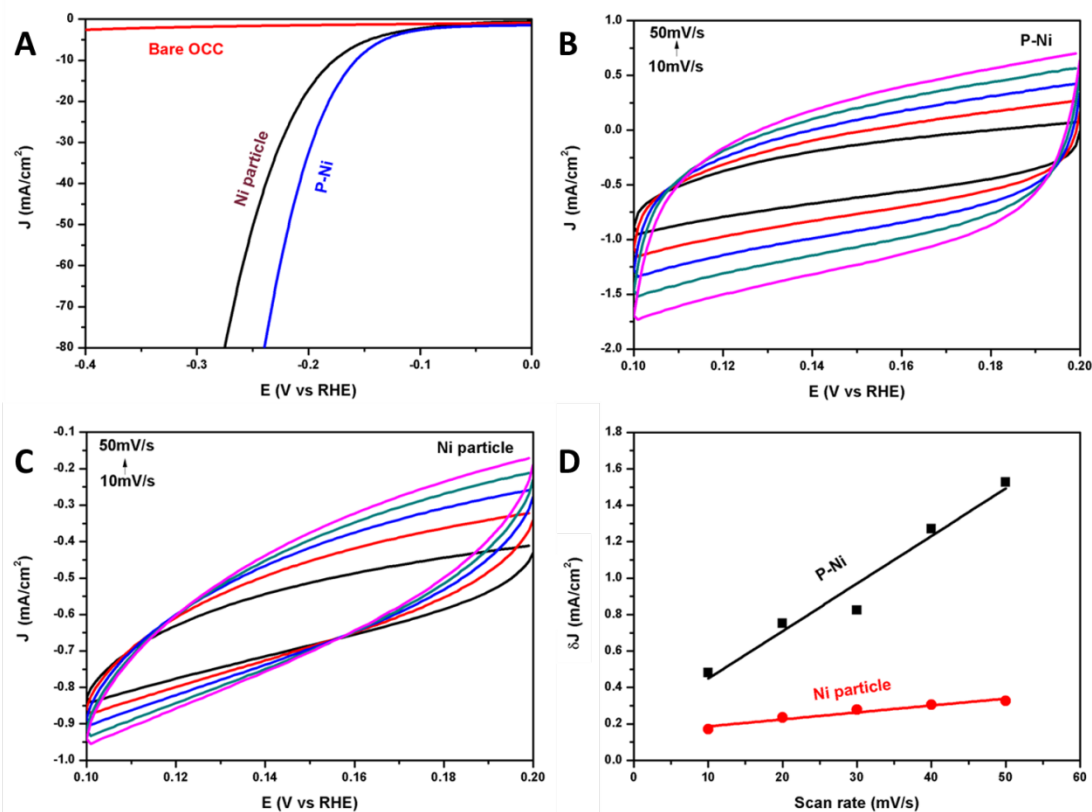
Figure 4. Electrochemical performance and electrochemical surface area (ECSA) test in alkaline electrolyte of 1 M KOH. A) Linear sweep voltammetry (LSV) curves of bare OCC, Ni particle on OCC, and P-Ni on OCC. B) CV curves of P-Ni and C) CV curves of Ni particle with variation of scan rates. D) charging current density differences-scan rates plot of Ni particle and P-Ni. Electrochemical surface area of P-Ni is larger than Ni particle, matching the same trend with electrocatalytic activity.
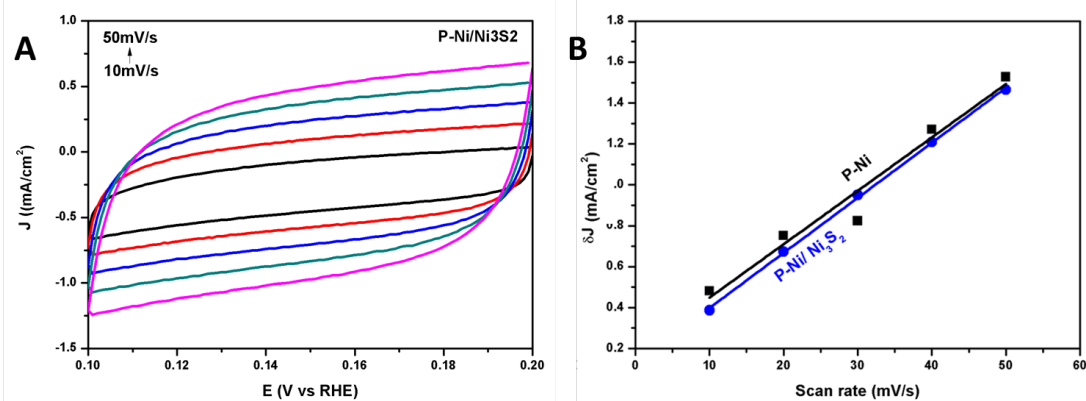
Figure 5. ECSA test in alkaline electrolyte of 1 M KOH. A) CV curves of P-Ni/Ni$_3$S$_2$ with variation of scan rates. B) charging current density differences-scan rates plot of P- Ni/Ni$_3$S$_2$ compared with P-Ni. P-Ni/Ni$_3$S$_2$ maintains the high ECSA with introduction of Ni$_3$S$_2$ on Ni network surface.

In order to further optimize the intrinsic catalytic activity of Ni-based material, we constructed Ni/Ni$_3$S$_2$ interface on the 3D porous Ni network, finely tuned the surface adsorption properties without decrease of ECSA. From Figure 5B, P-Ni/Ni$_3$S$_2$ shows similar double layer capacitance

value with 3D P-Ni, which is 2.69 uF, indicating surface area is slightly increased with sulfide modification.

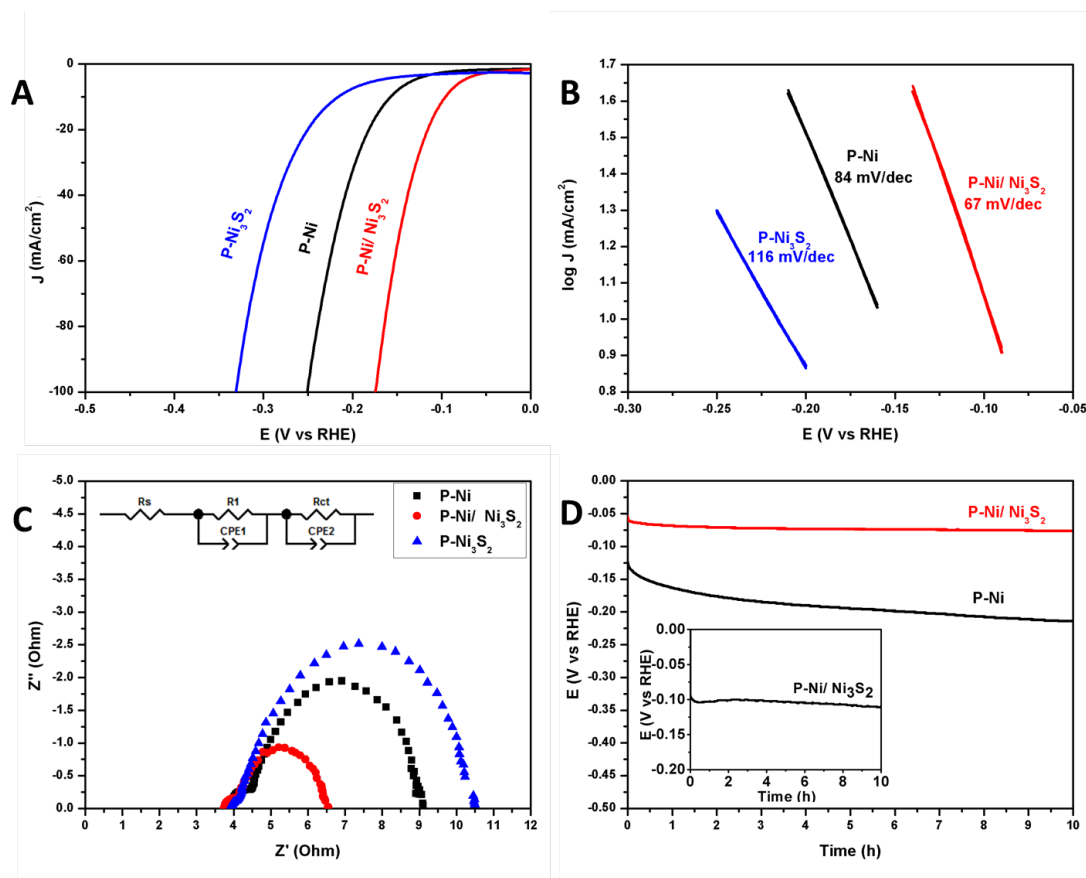Figure 6. Electrochemical performances of P-Ni/Ni$_3$S$_2$ compared with P-Ni and P-Ni$_3$S$_2$ on HER. A) LSV curves, B) Tafel plots, and C) electrochemical impedance spectra (EIS) at overpotential of 177 mV of P-Ni, P- Ni$_3$S$_2$, and P-Ni/Ni$_3$S$_2$ on OCC. D) chronopotentiometry test of P-Ni/Ni$_3$S$_2$ and P-Ni at current density of 5 mA/cm^2 (inset, CP test of P-Ni/Ni$_3$S$_2$ at current density of 10 mA/cm^2).

From the linear sweep voltammetry (LSV) curve of P-Ni/Ni$_3$S$_2$, 3D Ni and Ni$_3$S$_2$ catalyzed HER, it is clear that the potential applied to achieve the current density of 10 mA/cm^2 is positively shifted from 217 mV for P-Ni$_3$S$_2$ to 158 mV for P-Ni to 95 mV for P-Ni/Ni$_3$S$_2$. The much smaller overpotential of P-Ni/Ni$_3$S$_2$ confirms the strong synergistic effect induced higher HER activity than any individual part of pure Ni or pure Ni$_3$S$_2$. To further confirm the importance of Ni and Ni$_3$S$_2$ interface, Ni$_3$S$_2$ grown on P-Ni and Ni foam are synthesized for comparison. These two structures are obtained using hydrothermal growth of Ni$_3$S$_2$ sheets on P-Ni or Ni foam (NF), getting metal Ni and Ni$_3$S$_2$ in two steps, leaving barely no Ni/Ni$_3$S$_2$ interface, which is different from getting Ni and Ni$_3$S$_2$ at the same time from Ni(OH)$_x$S$_y$ reduction. Obviously, the overpotentials are much larger than P-Ni/Ni$_3$S$_2$, nearly 200 mV are needed at current density of 10 mA/cm^2 for both NF/Ni$_3$S$_2$ and P-Ni/Ni$_3$S$_2$ sheets (Figure S7), indicating the effectiveness of synergistic effect between Ni and Ni$_3$S$_2$ interface. Impressively, P-Ni/Ni$_3$S$_2$ also shows good catalytic activity in neutral environment, exhibiting 196 mV low overpotential at current density of 10 mA/cm^2, and tafel slope of 170 mV/dec in pH 7 phosphate buffer solution (Figure S5).

Tafel slope was measured to determine HER kinetics. The tafel slope of P-Ni/Ni$_3$S$_2$ is 67 mV/dec,

while P-Ni and P-Ni$_3$S$_2$ exhibit relatively higher tafel slope, which is 84 mV/dec and 116 mV/dec, respectively. The small tafel slope confirms the advantage of the 3D porous structure. This structure is beneficial for exposing more active sites to electrolyte as well as facilitating mass transfer during the reaction. Additionally, highly conductive Ni network inside makes charge transfer easier, which helps speeding up the reaction as a result. Low tafel slope of P-Ni/Ni$_3$S$_2$ reveals the fast reaction kinetic toward hydrogen production, quickly reaching high current density in relative low overpotential.

The rapid reaction kinetics of P-Ni/Ni$_3$S$_2$ is further verified by electrochemical impedance spectroscopy (EIS). Nyquist plots of P-Ni, P-Ni$_3$S$_2$ and P-Ni/Ni$_3$S$_2$ measured at overpotential of 120 mV are shown in Figure 6C. The equivalent circuit consists of a solvent resistance (R_s), and two parallel resistances (R_1, R_{ct}) with constant phase element (CPE$_1$, CPE$_2$). The similar R_s values of P-Ni (R_s=3.75 Ω), P-Ni$_3$S$_2$ (R_s=3.94 Ω) and P-Ni/Ni$_3$S$_2$ (R_s=3.92 Ω) demonstrated in EIS data reveal the Ohmic resistance for all the contact in the three materials including interface with electrolyte are nearly the same. R_{ct} can be related with charge transfer at the catalyst-electrolyte interface. P-Ni$_3$S$_2$ (R_{ct}=2.42 Ω) shows faster charge transfer kinetics compared with P-Ni (R_{ct}=4.54 Ω) and P-Ni$_3$S$_2$ (R_{ct}=6.31 Ω), which is in accordance with the smaller overpotential of P-Ni/Ni$_3$S$_2$. The high conductivity and fast charge transfer kinetics provided by the intrinsic metallicity of Ni$_3$S$_2$ facilitate the HER electrocatalysis. It leads to an easier charge sustain process and Ohmic contact between catalyst and electrolyte interface, instead of additional schottky barrier needed to conquer for lots of HER catalysts.

As a critical criterion for electrocatalysis, durability of P-Ni and P-Ni/Ni$_3$S$_2$ are tested in 1.0 M KOH solution. We test it by chronopotentiometry at the current density of 5 mA/cm^2 for 10 h. As it is demonstrated in Figure 6D, very small potential shift needed to reach 5 mA/cm^2 is observed for P-Ni/Ni$_3$S$_2$, while P-Ni shows more obvious stability decrease as it is observed by other groups. The reason might be: 1) OH species generated on the P-Ni/Ni$_3$S$_2$ interface could be removed by Ni$_3$S$_2$ from Ni, avoiding interaction between Ni and OH or the blocking of Ni active sites. 2) optimized adsorption/desorption energy makes Ni/Ni$_3$S$_2$ interface form less NiH irreversible species than Ni metal. Chronopotentiometry test for P-Ni/Ni$_3$S$_2$ at 10 mA/cm^2 is also conducted for 10 h, proving the good stability of 3D Ni$_3$S$_2$ modified Ni structure.

HER mechanism and computational support

Instead of the direct proton involvement, HER in alkaline solution comprises discharge of water (M + H$_2$O + e$^-$ $\rightarrow$ MH$_{ad}$ + OH$^-$), followed by a second electron transfer (H$_2$O + MH$_{ad}$ + e$^-$ $\rightarrow$ M + H$_2$ + OH$^-$), or 2MH$_{ad}$ $\rightarrow$ 2M + H$_2$. According to the result presented above, we propose that the reaction proceeds via the mechanism schematically illustrated in Figure 7.
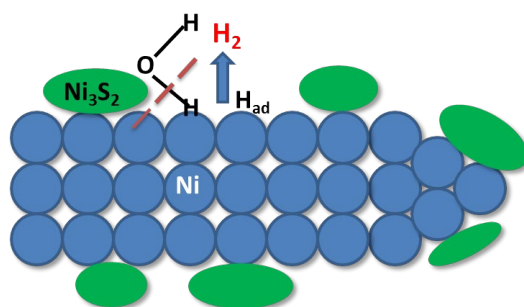
Figure 7. Schematic illustration of HER mechanism on P-Ni/Ni$_3$S$_2$ interface.

Specifically, the water splitting reaction happens at the Ni and Ni$_3$S$_2$ interface. Small grains of Ni$_3$S$_2$ grown on Ni surface help to dissociate water molecule. The relatively electron-rich oxygen atoms in water molecules prefer to adsorb on Ni$_3$S$_2$ because of its high coordinating ability to positively charged Ni$^+$ and Ni^{2+} in Ni$_3$S$_2$, while hydrogen preferentially adsorb on Ni surface. The O-H bond in water molecule breaks at the Ni/Ni$_3$S$_2$ interface, producing H$_{ad}$ absorbed on Ni sites, because of the suitable hydrogen atom binding energy with Ni metal. The adsorbed hydrogen atom (H$_{ad}$) recombine with another H$_{ad}$, or go through a second electron transfer to generate hydrogen molecule.

We have conducted density functional theory (DFT) calculation to support the catalytic mechanism stipulated above. To approach the experimental conditions in more detail, we have built two different interface models (model 1 and 2) as shown in Figure 8, based on the supercell structure as introduced by one of our previous collaborators [25]. These two interface models result in two different interface bonding characteristics with Ni$_3$S$_2$ (111) surface. We see from Figure 8 that the interface Ni sites are obviously relaxed into a region that deviated from either Ni$_3$S$_2$ or Ni metal lattice due to strong Ni-S bonding as the bond length of S-Ni at the interface is shortened. Some portions of Ni-metal surface have shown to be corrugated to accommodate the Ni-S bonds. The main lattices of Ni$_3$S$_2$ and Ni-metal are relatively rigid with less distortion. The semi-core 3d orbitals and the strong valence-core overlapping effects have been self-consistently corrected, see Figure S8 for the procedure of determining the screened Coulomb potentials on the targeted orbitals.
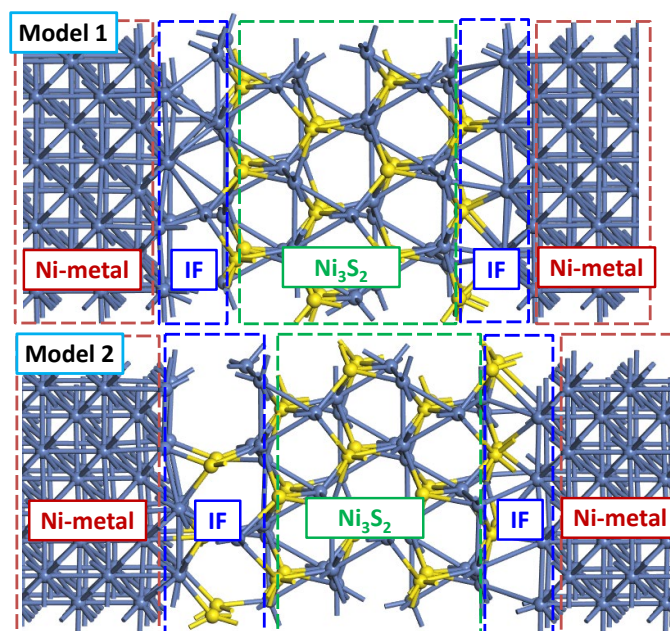

Figure 8. Two interface bonding models are built combining Ni$_3$S$_2$ (111) surface and pure Ni metal part. The interface in model 1 contains both Ni-rich and S-rich bonding, and the model 2 has the S-rich bonding only.

We built two different interface models for simulating the water splitting process and

energetics, as shown in Figure 8. These models differ on the interface bonding between Ni and S sites. For model 1, it contains both Ni-rich (Ni-Ni) and S-rich (S-Ni) bonding between Ni_3S_2 and Ni metal parts. While for model 2, it has the S-rich (S-Ni) bonding only. To determine the H_2O initial structural configuration and the location of its insertion into the as-synthesized samples, we performed a preliminary molecular dynamics (MD) simulation under standard room temperature (300 K) with NVT ensembles, meaning that the dynamic simulation is carried out at fixed volume with a thermostat to maintain a constant temperature. The MD simulations on H_2O penetrations were attempted on three different parts, which are pure Ni metal, interface region, and Ni_3S_2. They are found to merge in the interface region during the MD steps. From our transition energy and electronic property calculations at the Ni/Ni_3S_2 interfaces, we found that stabilization of H_2O within the interface region is only an intermediate step, during which the O-Ni long and weak bonding was established. In more detail, the local structure of H in H_2O within the interface layer is such that pointing to the pure Ni metal surface is energetically preferred to the opposite.
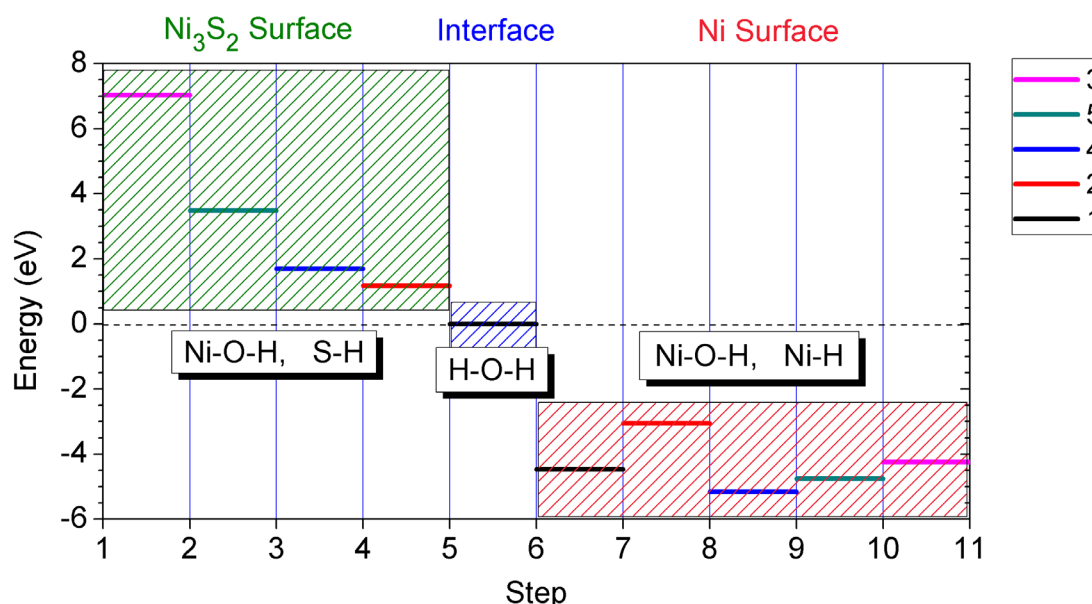

Figure 9. Transition energy levels of one single H_2O splitting/hydrogen evolution process in the Ni/Ni_3S_2 interface system. The energy levels shown in steps 1-6 denote the relative energy of initial relaxed structures of H_2O on the Ni_3S_2 surface, compared to the H_2O staying within the interface region (0 eV line). The energy levels shown in steps 6-11 are representing the energies of final relaxed structures, compared to the H_2O at the interface (0 eV line). The relative energy levels are further shown in pairs with sequence numbers from 1 to 5, shown in black, red, blue, olive green and pink, respectively. The [Ni-O-H, S-H] pair represents the local relaxed structure from H_2O initially interacting with the Ni_3S_2 surface, indicating an evident energy barrier to split H_2O. The [H-O-H] species shows the pristine H_2O molecule staying within the interface region. The [Ni-O-H, Ni-H] pair shows the final relaxed bonding structure after splitting H_2O with the formation of a new bond to the Ni metal surface. Different energy levels from 6-11 are representing the different inter-distances between hydroxyl (OH) and hydrogen (H) on the Ni-metal part surface at the final relaxed state. The 7-8 level is an exception which denotes a state has no bond breaking between the O and H in H_2O on the Ni-metal surface.

Figure 9 is a group of transition energy level diagrams that illustrate the trend of water splitting at such system. The left part (step 1-5) shows different initial relaxed structures for H2O locating on the Ni3S2 surface with bonding either Ni-O or Ni-H. The step 5-6 shows the level of an

intermediate energy state that H2O locating within the interface region. The 6-11 levels are the final relaxed energy levels that bonding with Ni at the Ni-metal part. Rather than staying in the region that bonding with either pure Ni metal or close contact with Ni_3S_2 surface (shown in Figure S13 and S14), the insertion of H_2O as well as the initial weak bonding reflects a subtle trade-off on the interactions between Ni metal and Ni_3S_2. The relative energetic difference is illustrated in Figure 9, in order to show the bonding contrast between both sides, i.e. Ni-metal and Ni_3S_2 sides, respectively. We performed the transition energy level calculation for verifying the initial starting and the final relaxed structural configurations by decomposing the water-splitting process into the steps given.

As confirmed by MD simulation, we set the total energy of the H_2O locating within the interface region to the 0 eV line, then pair-up the energy levels between the initially set and finally relaxed structures relative to the 0 eV configuration, as shown by the sequence 1-5 given in Figure 9. Accordingly, the H_2O locating on the Ni_3S_2 surface with different local structural configurations are actually the meta-stable states shown by the energy levels lined-up in form of staircase. However, the unusual energy contrast occurs to the final relaxed structures. Those different meta-stable states are uniformly relaxed to the even lower energy levels across the 0 eV (interface region) and finally form new and different bonds. The energy difference between different structural configurations gets lower when H_2O is transferred across the interface and split into OH and H on the Ni metal surface. The average energy level is generally 4 eV lower than the 0 eV reference (H_2O at the interface). Such a trend, clear shown in our calculation, indicates that the H_2O splitting process is finally taking place at the Ni metal surface, and the Ni_3S_2 surface is weakening the binding energy between the sample and H after the split of water. In addition, as shown in Figure S13, the bond breaking of H-O-H on Ni_3S_2 still requires an energy barrier of about 1.5~1.6 eV when H_2O locates on the Ni sites of the Ni_3S_2 surface (note the H_2O on S site is energetically unfavorable.). Thus, the high HER performance by water splitting is certainly associated with the existence of the Ni-Ni_3S_2 interface instead of Ni3S2 only.

As shown in Figure S15, we decompose the different energy levels into local structures in real space. By a comparison among the total energy levels, the highest energy structural configuration of the H_2O at the initial stage is near or bonded at the Ni_3S_2 surface. The total energies with considerations of local O-Ni, H-S, or H-Ni bonding are all uniformly high. This can be explained by a view of derived by Trasatti [26] with related to the work-function of d-orbital metal or d-orbital based solids. We will further illustrate the WF properties in the following discussion by bonding detail and interface potential gradient.

First, because of the localized non-bonding orbital such as long-pair electrons localized surface of the Ni_3S_2 given by the S sites, the Coulomb repulsive potential between long-pair electrons of S and O atoms from [H-Ö-H] units are over too strong. From the final ground state relaxed structures, it is showing that the H_2O has all been split into two parts like O-H and H deviated away from the interface region. The final O-H group has been bonded by the Ni site at the Ni metal surface. We have also carried out the MD simulation and shown that the O-H will be further split into O and H as we call secondary splitting potentially. Then the O is itinerant within the interface area or vacant region, and the rest H will be still bonded by the Ni site at the surface

of pure Ni metal part (see SI for more details). At the meanwhile, the calculation on PDOSs of d-orbitals shown in Figure S16 (b) presents a consistency with similar result observed in NiS-Ni_3S_2 interface system by experiment[27]. This actually demonstrates the change in oxidation state of the Ni site at the interface is also an important factor to influence the HER performance of as-synthesized samples.

Another concern is the role work functions (WF) of the Ni_3S_2 surface as well as the Ni-Ni_3S_2 interface system. According to the empirical relation derived by Trassati [26], the work function of the sample surface is linear relationship to the binding energy between the sample and H, and the larger work function the sample possesses, the weaker binding energy it has [26, 28, 29]. The HER performance was further derived to present to be higher [30]. Experimental measured work function (WF) for Ni_3S_2 is 5.11 eV [27], our DFT calculation on the Ni_3S_2 surface slab model gives the work function to be 5.084 eV, in close agreement with the experimental data. The WF of Ni_3S_2 is very comparable to the Pt (5.65 eV) [26] and thus may have a good HER performance. There is a slight difference between our calculated WF for Ni (4.516 eV) and literature reported (~4.7 eV) [26, 30]. This arises because the experimental measurement on WF can be obviously influenced by the sample substrate and absorbing impurities on the sample surface. Such difference can be negligible and still in a good physical trend. The WF for interface area we are focusing on is calculated and shows the value of 5.732 eV, which is very close to the WF of Pt (5.65 eV) [26].

As we know, the difference between the E_F levels for Ni_3S_2 and Ni metal parts would induce an internal Coulomb potential gradient, which can facilitate the electron transfer across the interface in a higher efficiency. Moreover, the potential gradient is seen to be a built-in electrical field that pushes the H_2O from higher electronic density to lower one due to the strong Coulomb repulsive potential between interface electrons and lone-pair electrons of O from H-Ö-H. Thus, an area with high catalytic activity is found to be locating at the interface between pure Ni and Ni_3S_2 nano-composite system. It has a remarkably high efficiency to splitting the water on the Ni metal surface facilitated by the Ni_3S_2 interfacial electrical potential gradient. This nano-interface of as synthesized Ni-Ni_3S_2 would suggest a potentially high HER performance for replacing the Pt-based catalyst[17], of which properties modulation can be tailor-made via a wider range than the noble metal catalysts.

Conclusion

We have devised a facile strategy for 3D porous Ni/Ni_3S_2 growth. The high activity of P-Ni/Ni_3S_2 could be attributed to the following reasons: firstly, strong synergetic effect between Ni and Ni_3S_2 at Ni/Ni_3S_2 interface leads to an optimized adsorption/desorption energy during HER process, promoted the intrinsic catalytic activity of Ni/NiS system from thermodynamic perspective as the reaction mechanism verified by DFT calculation. Secondly, the 3D porous structure processes high electrochemical surface area, exposing more active sites to electrolyte and facilitating mass transfer at the same time. Thirdly, the highly conductive Ni network inside associated with its good combination with Ni_3S_2 on the surface make charge transfer easier, and consequently speed up the reaction for hydrogen evolution. In brief, Ni_3S_2 plays a critical role in assisting Ni metal for water reduction, and the effectiveness of constructing 3D porous Ni/Ni_3S_2 nano-interfaces makes

the electrocatalytic property toward HER in alkaline and neutral solution outperform traditional Ni material currently used in industry. On the basis of our DFT calculation analysis, the 3d orbital level shifting from Ni-metal, interface to the Ni_3S_2 is about 1 eV in magnitude, which supportively shows the change of the oxidation states of Ni sites of three different parts. The Ni site on Ni_3S_2 still requires an energy barrier to perform a bond breaking on H-O-H unit, and Ni-H is strong on the Ni metal surface. With interface assistance, the bond breaking effect takes place through a path towards to a potential well instead of barrier. The difference of work function arise from the d-orbital level variation shows an internal electrical potential gradient to suppress the H2O splitting on the Ni metal surface but with weaker binding between Ni-H. This energy reduction is resulted from an evident energy lowering (~4 eV) for H_2O splitting on the Ni metal surface associated by the interface.

Acknowledgment

Reference

[1]   I. Roger, M. A. Shipman, and M. D. Symes, Nature Reviews Chemistry **1**, 0003 (2017).

[2]   N. P. Dasgupta, C. Liu, S. Andrews, F. B. Prinz, and P. Yang, Journal of the American Chemical Society **135**, 12932 (2013).

[3]   T. R. Cook, D. K. Dogutan, S. Y. Reece, Y. Surendranath, T. S. Teets, and D. G. Nocera, Chemical reviews **110**, 6474 (2010).

[4]   Y. Li, H. Wang, L. Xie, Y. Liang, G. Hong, and H. Dai, Journal of the American Chemical Society **133**, 7296 (2011).

[5]   D. Voiry, et al., Nature materials **12**, 850 (2013).

[6]   H. Zhou, Y. Wang, R. He, F. Yu, J. Sun, F. Wang, Y. Lan, Z. Ren, and S. Chen, Nano Energy **20**, 29 (2016).

[7]   E. J. Popczun, C. G. Read, C. W. Roske, N. S. Lewis, and R. E. Schaak, Angewandte Chemie **126**, 5531 (2014).

[8]   E. J. Popczun, J. R. McKone, C. G. Read, A. J. Biacchi, A. M. Wiltrout, N. S. Lewis, and R. E. Schaak, Journal of the American Chemical Society **135**, 9267 (2013).

[9]   T. Schmidt, P. Ross, and N. Markovic, Journal of Electroanalytical Chemistry **524**, 252 (2002).

[10]   D. Hall, Journal of The Electrochemical Society **128**, 740 (1981).

[11]   K. Zeng and D. Zhang, Progress in Energy and Combustion Science **36**, 307 (2010).

[12]   M. Janjua and R. Le Roy, International Journal of Hydrogen Energy **10**, 11 (1985).

[13]   N. Danilovic, R. Subbaraman, D. Strmcnik, K. C. Chang, A. Paulikas, V. Stamenkovic, and N. M. Markovic, Angewandte Chemie **124**, 12663 (2012).

[14]   M. Gong, et al., Nature communications **5** (2014).

[15]   J. R. McKone, B. F. Sadtler, C. A. Werlang, N. S. Lewis, and H. B. Gray, ACS Catalysis **3**, 166 (2013).

[16]   D. Merki and X. Hu, Energy & Environmental Science **4**, 3878 (2011).

[17]   G. F. Chen, T. Y. Ma, Z. Q. Liu, N. Li, Y. Z. Su, K. Davey, and S. Z. Qiao, Advanced Functional

Materials **26**, 3314 (2016).

[18]   Y. Wu, G. D. Li, Y. Liu, L. Yang, X. Lian, T. Asefa, and X. Zou, Advanced Functional Materials (2016).

[19]   S. Peng, et al., Angewandte Chemie **126**, 12802 (2014).

[20]   L.-L. Feng, G. Yu, Y. Wu, G.-D. Li, H. Li, Y. Sun, T. Asefa, W. Chen, and X. Zou, Journal of the American Chemical Society **137**, 14023 (2015).

[21]   W. Zhou, X.-J. Wu, X. Cao, X. Huang, C. Tan, J. Tian, H. Liu, J. Wang, and H. Zhang, Energy & Environmental Science **6**, 2921 (2013).

[22]   X. Long, G. Li, Z. Wang, H. Zhu, T. Zhang, S. Xiao, W. Guo, and S. Yang, Journal of the American Chemical Society **137**, 11900 (2015).

[23]   K. Krishnamoorthy, G. K. Veerasubramani, S. Radhakrishnan, and S. J. Kim, Chemical Engineering Journal **251**, 116 (2014).

[24]   N. Feng, D. Hu, P. Wang, X. Sun, X. Li, and D. He, Physical Chemistry Chemical Physics **15**, 9924 (2013).

[25]   K.-Y. Tse and J. Robertson, Phys. Rev. Lett. **99**, 086805 (2007).

[26]   S. Trasatti, Journal of Electroanalytical Chemistry and Interfacial Electrochemistry **39**, 163 (1972).

[27]   Y. Liao, K. Pan, Q. Pan, G. Wang, W. Zhou, and H. Fu, Nanoscale **7**, 1623 (2015).

[28]   Y. Jiao, Y. Zheng, M. Jaroniec, and S. Z. Qiao, Chem. Soc. Rev. **44**, 2060 (2015).

[29]   F. Calle-Vallejo, M. T. M. Koper, and A. S. Bandarenka, Chem. Soc. Rev. **42**, 5210 (2013).

[30]   A. R. Zeradjanin, J.-P. Grote, G. Polymeros, and K. J. J. Mayrhofer, Electroanal. **28**, 2256 (2016).